J|A|C|S
ARTICLES

Nanostructures versus Solid Solutions: Low Lattice Thermal Conductivity and Enhanced Thermoelectric Figure of Merit in $Pb_{9.6}Sb_{0.2}Te_{10-x}Se_x$ Bulk Materials

Pierre F. P. Poudeu,[†,∥] Jonathan D'Angelo,[‡] Huijun Kong,[§] Adam Downey,[‡]
Jarrod L. Short,[‡] Robert Pcionek,[†] Timothy P. Hogan,[‡] Ctirad Uher,[§] and
Mercouri G. Kanatzidis*[,†,∥]

*Contribution from the Department of Chemistry, Michigan State University,
East Lansing, Michigan 48824, Department of Electrical and Computer Engineering,
Michigan State University, East Lansing, Michigan 48824, and Department of Physics,
University of Michigan, Ann Arbor, Michigan 48109*

Received July 5, 2006; E-mail: m-kanatzidis@northwestern.edu

Abstract: The series of $Pb_{9.6}Sb_{0.2}Te_{10-x}Se_x$ compounds with different Se content (x) were prepared, and their structure was investigated at the atomic and nanosized regime level. Thermoelectric properties were measured in the temperature range from 300 to 700 K. The $Pb_{9.6}Sb_{0.2}Te_{10-x}Se_x$ series was designed after the refinement of the single-crystal structure of $Pb_{3.82}Sb_{0.12}Te_4$ ($Pb_{9.6}Sb_{0.3}Te_{10}$; S.G. $Pm\bar{3}m$) by substituting isoelectronically in anion positions Te by Se. The $Pb_{9.6}Sb_{0.2}Te_{10-x}Se_x$ compounds show significantly lower lattice thermal conductivity (κ_L) compared to the well-known $PbTe_{1-x}Se_x$ solid solutions. For $Pb_{9.6}Sb_{0.2}Te_3Se_7$ ($x = 7$), a κ_L value as low as 0.40 W/m·K was determined at 700 K. High-resolution transmission electron microscopy of several $Pb_{9.6}Sb_{0.2}Te_{10-x}Se_x$ samples showed widely distributed Sb-rich nanocrystals in the samples which is the key feature for the strong reduction of the lattice thermal conductivity. The reduction of κ_L results in a significantly enhanced thermoelectric figure of merit of $Pb_{9.6}Sb_{0.2}Te_{10-x}Se_x$ compared to the corresponding $PbTe_{1-x}Se_x$ solid solution alloys. For $Pb_{9.6}Sb_{0.2}Te_3Se_7$ ($x = 7$), a maximum figure of merit of $ZT \approx 1.2$ was obtained at $\sim$650 K. This value is about 50% higher than that of the state-of-the-art n-type PbTe. The work provides experimental validation of the theoretical concept that embedded nanocrystals can promote strong scattering of acoustic phonons.

Introduction

New materials with an enhanced thermoelectric figure of merit (ZT) are now the target of widespread investigations. Solid state thermoelectric devices can be used as direct heat to electricity converters (power generation) or as coolers by using electricity to pump heat from a cold side to a hot side. The figure of merit ZT is defined as $ZT = (\sigma S^2)T/\kappa$, where S is the Seebeck coefficient, σ is the electrical conductivity, κ is the total thermal conductivity, and T is the absolute temperature. Improved figure of merit can be achieved by lowering the thermal conductivity while avoiding significant deterioration of the electrical conductivity and Seebeck coefficient. One good way to do so is to engineer the lattice part of the total thermal conductivity. In solid solutions such as $PbTe_{1-x}Se_x$,[1] atomic substitutions scatter short-wavelength phonons due to differences in mass, thereby reducing the lattice thermal conductivity. Low dimensional structures such as PbTe-based superlattice thin-films[2−7] and quantum dot superlattices[8−10] have been reported to produce improved thermoelectric figure of merit due to phonon confinement and enhanced phonon scattering that result in lower lattice thermal conductivity. It is now believed that low lattice thermal conductivity can also be achieved by nanocrystalline inclusions embedded in bulk materials.[11−15]

[†] Department of Chemistry, Michigan State University.
[‡] Department of Electrical and Computer Engineering, Michigan State University.
[§] University of Michigan.
[∥] Current address: Department of Chemistry, Northwestern University, 2145 Sheridan Road, Evanston, IL 60208.

(1) Devyatkova, E. D.; Tikhonov, V. V. *Sov. Phys. Solid State* **1965**, *7*, 1427−1431.
(2) Venkatasubramanian, R.; Colpitts, T.; Watko, E.; Lamvik, M.; El-Masry, N. *J. Cryst. Growth* **1997**, *170*, 817−821.
(3) Harman, T. C.; Spears, D. L.; Manfra, M. J. *J. Electron. Mater.* **1996**, *25*, 1121−127.
(4) Aigle, M.; Pascher H.; Kim H.; Tarhan E.; Mayur A. J.; Sciacca M. D.; Ramdas A. K.; Springholz G.; Bauer G. *Phys. Rev. B* **2001**, *64*, 35316.
(5) Caylor, J. C.; Coonley, K.; Stuart, J.; Colpitts, T.; Venkatasubramanian, R. *Appl. Phys. Lett.* **2005**, *87*, 23105.
(6) Beyer, H.; Nurnus, J.; Boettner, H.; Lambrecht, A.; Roch, T.; Bauer, G. *Appl. Phys. Lett.* **2002**, *80*, 1216−1218.
(7) Boettner, H.; Chen, G.; Venkatasubramanian, R. *MRS Bulletin* **2006**, *31*, 211−217.
(8) Harman, T. C.; Spears, D. L.; Walsh, M. P. *J. Electron. Mater.* **1999**, *28*, L1−L4.
(9) Harman, T. C.; Taylor, P. J.; Spears, D. L.; Walsh, M. P. *18th International Conference on Thermoelectrics* **1999**, 280−284.
(10) Harman, T. C.; Taylor, P. J.; Walsh, M. P.; LaForge, B. E. *Science* **2002**, *297*, 2229−2232.
(11) (a) Hsu, K. F.; Loo, S.; Guo, F.; Chen, W.; Dyck, J. S.; Uher, C.; Hogan, T.; Polychroniadis, E. K.; Kanatzidis, M. G. *Science* **2004**, *303*, 818−821. (b) Quarez, E.; Hsu, K.-F.; Pcionek, R.; Frangis, N.; Polychroniadis, E. K.; Kanatzidis M. G. *J. Am. Chem. Soc.* **2005**, *127*, 9177−9190.
(12) Nolas, G. S., Poon, J., Kanatzidis, M. G. *MRS Bulletin* **2006**, *31*, 199−205.
(13) Kim, W.; Zide, J.; Gossard, A.; Klenov, D.; Stemmer, S.; Shakouri, A.; Majumdar, A. *Phys. Rev. Lett.* **2006**, *96*, 045901.

10.1021/ja0647811 CCC: $33.50

Our investigation of the thermoelectric properties of the $Pb_{9.6}Sb_{0.2}Te_{10-x}Se_x$ system was motivated by a recent theoretical study of the effect of Sb impurities on the electronic structure of PbTe which indicated additional electronic states at the bottom of the conduction band.[16] This suggests a possible enhancement of the thermopower for optimal Sb concentration. In addition, the investigation of phonon scattering in the $PbTe_{1-x}Se_x$[1] solid solution revealed a significant reduction of the lattice part of the thermal conductivity (for optimum Se concentration) due to large mass fluctuation in the crystal lattice. Given the low solubility of Sb in the PbTe lattice,[17] we anticipated a phase separation upon cooling with formation of Sb precipitates embedded in a $Pb_{9.6}Sb_zTe_{10-x}Se_x$ ($z < 0.2$) matrix. Such precipitates could play a key role in reducing the lattice thermal conductivity through the scattering of midwave-length to long wavelength phonons.[13]

Here we report a strong reduction of the lattice thermal conductivity and an enhanced thermoelectric figure of merit for n-type $Pb_{9.6}Sb_{0.2}Te_{10-x}Se_x$ materials. The effect of the variation of Se content on the lattice thermal conductivity of $Pb_{9.6}Sb_{0.2}Te_{10-x}Se_x$ solid solution and its juxtaposition to the effect of nanostructuring in these materials is discussed. Single-crystal X-ray refinements coupled with high-resolution transmission electron microscopy (HRTEM) images of selected samples show that the Sb both is dissolved in the $PbTe_{1-x}Se_x$ lattice (occupying the Pb positions) and also nucleates as a second phase forming Sb-rich nanocrystals distributed inside $PbTe_{1-x}Se_x$-rich matrix. We show here that the nanocrystals are responsible for the very low lattice thermal conductivity of $Pb_{9.6}Sb_{0.2}Te_{10-x}Se_x$ materials. To derive meaningful conclusions about the role of nanostructures, lattice thermal conductivity values of $Pb_{9.6}Sb_{0.2}Te_{10-x}Se_x$ materials are compared with those of the well-known $PbTe_{1-x}Se_x$[1] solid solution alloys. The latter do not exhibit any nanostructuring. We report a very large reduction in the lattice thermal conductivity which is due to the formation of Sb-rich nanocrystals inside the bulk crystal and provides an additional phonon scattering mechanism over and above the standard point defect scattering mechanism that typically governs solid solutions. To fully characterize the thermoelectric performance of $Pb_{9.6}Sb_{0.2}Te_{10-x}Se_x$ materials, electrical conductivity and thermopower were also measured. Selected compositions exhibited a marked improvement in the figure of merit (e.g., $ZT = 1.2$ at 650 K for $x = 7$) as a result of their very low thermal conductivity. This is about 50% higher than that of the state-of-the-art n-type PbTe.

Experimental Procedure

Synthesis. $Pb_{9.6}Sb_{0.2}Te_{10-x}Se_x$ ($x = 0$ to 10) samples used in the present study were prepared as polycrystalline ingots using elemental Pb (99.99%), Sb (99.999%), Te (99.999%), and Se (99.999%). The starting compositions (nominal) were calculated based on the general formula. All four components weighed in the desired ratio (total mass ≈ 20 g) under ambient atmosphere were transferred into quartz tubes ($\varnothing = 13$ mm, Length = 20 cm) and flame-sealed under a residual pressure of $\sim 10^{-4}$ Torr. The sealed tubes were placed into a tube furnace (mounted on a rocking table) and heated to allow complete melting of all components at 1250 K. While molten the furnace was allowed to rock to facilitate complete mixing and homogeneity of the liquid phase. After several hours of rocking, the furnace was finally immobilized at the vertical position for the crystal growth. The furnace was slowly cooled from 1250 to 820 K in 43 h followed by a fast cool to room temperature. The resulting polycrystalline ingot was air-stable with color varying from lustrous silver-like (low value of x) to dark gray (high value of x).

DTA Analysis. Differential thermal analyses (DTA) were performed with a Shimadzu DTA-50 thermal analyzer. Approximately 30 mg of finely ground powder of the materials was sealed in a quartz ampule under reduced pressure. An equivalent mass of alumina (Al_2O_3) was sealed in an identical ampule to serve as reference. The samples were heated to 1000 °C at a rate of 10 °C/min, isothermed for 2 min and then cooled to 150 °C at a rate of 10 °C/min. The temperature difference between the sample and the reference was monitored during two heating and cooling cycles.

Powder X-ray Diffraction. $Pb_{9.6}Sb_{0.2}Te_{10-x}Se_x$ fine powder samples were examined by X-ray diffraction. Diffraction patterns were collected using a Cu K_α ($\lambda = 1.540\,56$ Å) radiation in reflection geometry on an Inel diffractometer equipped with a position sensitive detector and operating at 40 kV and 20 Amp.

Single-Crystal X-ray Diffraction. Single crystals of $Pb_{3.82}Sb_{0.12}Te_4$ were obtained by evaporation during the synthesis of polycrystalline samples. Intensity data were recorded using graphite monochromatized Mo Kα ($\lambda = 0.710\,73$ Å) radiation on a STOE IPDS-II diffractometer. The data set was corrected for Lorentz and polarization effects. Analytical absorption correction based on face indexing crystal description was applied using the program XRED.[18] Prior to the absorption correction, the crystal shape was optimized using a set of equivalent reflections and the program X-SHAPE.[19] For the structure refinement we employed the SHELXTL[20] package of programs.

To determine the correct symmetry of the crystal, the *hk*0 precession photograph was simulated using the diffraction data and the program BuildSpace[21] from the STOE IPDS-II package of programs. The simulated photograph showed additional spots violating the expected F lattice. The supplementary reflections were successfully indexed in the lower symmetry primitive lattice. The structure was successfully solved and refined[20] in the space group $Pm\bar{3}m$ (No. 221). Two crystallographically independent metal positions and two anion positions were determined. As a starting model, all metal positions were assigned to Pb and the anion positions were assigned to Te. The structure was refined to a residual value $R1$ of about 11% using this model. This value dropped to about 6% after absorption correction and inclusion of anisotropic displacement parameters for all atoms in the structure. At this stage the difference electron density was very high (+9.10 and −7.07 e/Å^3), and the thermal parameter of M1(Pb1) was about twice that of M2(Pb2). This suggested a mixed occupancy between Pb and a lighter element at the M1 position. In further stages of the refinement, the M1 position was set to be mixed occupied by Pb and Sb. Both atoms were constrained to have the same displacement parameter. The site occupation factor was restrained to maintain the electroneutrality of the compound. Refinement of this model yielded a satisfactory description for the M1(Pb1/Sb1) atom and an almost flat difference electron density map. The following composition was obtained: M1 = 82% Pb + 12% Sb corresponding to a total occupancy of 94%. The formula of the compound based on this refinement was $Pb_{3.82(2)}Sb_{0.12(2)}Te_4$.

---

(14) Poudeu, P. F. P.; D'Angelo, J.; Downey, A. D.; Short, J. L.; Hogan, T. P.; Kanatzidis, M. G. *Angew. Chem., Int. Ed.* **2006**, *45*, 3835−3839.

(15) Androulakis, J.; Hsu, K. F.; Pcionek, R.; Kong, H.-J.; Uher, C.; D'Angelo, J. J.; Downey, A.; Hogan, T.; Kanatzidis, M. G. *Adv. Mater.* **2006**, *18*, 1170−1173.

(16) Mahanti, S. D.; Bilc, D. *J. Phys.: Condens. Matter* **2004**, *16*, S5277 − S5288.

(17) Abrikosov, N. Kh.; Skudnova, E. V.; Poretskaya, L. V.; Osipova, T. A. *Inorg. Mater.* **1969**, *5*, 630−633.

(18) *X-RED32, Data Reduction for STADI 4 and IPDS*, version 1.22; Stoe & Cie GmbH: Darmstadt, Germany, 2001.

(19) *X-SHAPE, Crystal Optimization for Numerical Absorption Correction*, version 1.06; Stoe & Cie GmbH; Darmstadt, Germany, 1999.

(20) Sheldrick, G. M. *SHELXLTL NT*, version 5.1; Bruker Analytical X-ray System: 1998.

(21) *BUILDSPACE, Program for viewing reciprocal layers*, version 1.01; Stoe & Cie: Darmstadt, Germany, 2003.

Table 1. Selected Crystallographic Data and Details of Structure Refinement for $Pb_{3.82}Sb_{0.12}Te_4$

formula	$Pb_{3.82}Sb_{0.12}Te_4$
formula weight [g/mol]	1316.5
crystal system; space group	cubic; $Pm\bar{3}m$ (no. 221)
crystal size [mm^3]; color	$0.24 \times 0.19 \times 0.13$; black
density (ρ_{cal}) [g/cm^3]	8.19
lattice parameters	refined from the total collected single-crystal reflections
a [Å]	6.440(1)
V [Å^3]; Z	267.1(1); 1
radiation [Å]	λ(Mo Kα) = 0.710 73
temperature [K]	293(1)
$2\theta_{max}$; index range	66.6°; $-9 \leq h, k, l \leq 9$
measured reflections	6364
unique reflections	127
reflec. with $F_o > 4\sigma(F_o)$	112
R_{int}/R_σ	0.070/0.014
absorption correction	numerical, crystal description optimized using equivalent reflections
μ [cm^{-1}]	710
transmission factors	0.0033 to 0.0413
structure refinement	least-squares method; full matrix; based on F^2; anisotropic displacement parameters
difference electron density [e/Å^3]	+0.77 to −1.48
$R_1(F_o > 4\sigma(F_o))^a$	0.019
wR_2(all)^b	0.036
GOF	0.935

[a] $R_1 = \Sigma||F_o| - |F_c||/\Sigma|F_o|$. [b] $wR_2 = \{\Sigma w(F_o^2 - F_c^2)^2/\Sigma[w(F_o^2)^2]\}^{1/2}$.

Table 2. Atomic Coordinates and Isotropic Displacement Parameters (Å$^2 \times 10^4$) for $Pb_{3.82}Sb_{0.12}Te_4$

atoms	*Wyck.*	occupancy	*x*	*y*	*z*	$U_{eq}{}^a$
Pb1	1*b*	0.82(1)	$^1/_2$	$^1/_2$	$^1/_2$	333(3)
Sb1	1*b*	0.12(1)	$^1/_2$	$^1/_2$	$^1/_2$	333(3)
Pb2	3*d*	1	$^1/_2$	0	0	237(2)
Te1	3*c*	1	$^1/_2$	$^1/_2$	0	184(2)
Te2	1*a*	1	0	0	0	174(3)

[a] U_{eq} is defined as one-third of the trace of the orthogonalized U^{ij} tensor.

Additional crystallographic data and details of the structure refinement are given in Table 1. The fractional atomic coordinates and isotropic displacement parameters of all atoms with estimated standard deviations are listed in Table 2.

Infrared Spectroscopy. Room temperature optical diffuse reflectance measurements were performed on finely ground powder samples with compositions $Pb_{9.6}Sb_{0.2}Te_{10-x}Se_x$ ($x = 0$ to 10) to probe the optical energy band gap of the series. The spectra were monitored in the mid-IR region (6000−400 cm^{-1}) with a Nicolet MAGNA-IR 750 spectrometer equipped with a collector diffuse reflectance of Spectra-Tech Inc. Absorption (α/S) data were calculated from reflectance data using the Kubelka−Munk function.[22] The optical band gaps were derived from α/S versus E (eV) plots.

Electrical Properties. Rectangular shape samples with typical sizes of 7 mm × 5 mm × 4 mm were employed to simultaneously measure electrical conductivity and thermoelectric power using a four-sample measurement system.[23,24] To fully characterize the figure of merit, the properties were measured for each sample over the selective temperature range of interest. To alleviate offset error voltages and increase the density of data points, a slow-ac technique was used with a heater pulse period of 720 s. The pulse shape was monitored, in situ, to determine temperature stabilization, and the sample chamber was maintained at a pressure of less than 10^{-5} Torr for the entire measurement run. All measurements were performed on a measurement system with capabilities up to 700 K, employing single-ended thermocouples for concurrently monitoring the temperature gradient and voltage gradient on the sample. Data acquisition and computer control of the system were maintained under the LabVIEW[25] software environment.

Thermal Conductivity. The thermal conductivity (κ) was determined as a function of temperature from room temperature to 800 K using the flash diffusivity method (FLashLine 5000, Anter Corp.). The front face of a small disc-shaped sample ($\varnothing = 8$ mm; thickness $\approx$ 1−2 mm) is irradiated by a short laser burst, and the resulting rear face temperature rise is recorded and analyzed. Thermal conductivity (κ) values were calculated using the equation $\kappa = \alpha C_p d$, where α is the thermal diffusivity, C_p is the specific heat (measured using differential scanning calorimetry), and d is the bulk density of the sample (calculated from the sample's geometry and mass).

Lattice thermal conductivities were obtained by subtracting the carrier contribution from the total thermal conductivity using the equation $\kappa_{(lattice)} = \kappa_{(total)} - \kappa_{(carrier)}$. Here, $\kappa_{(carrier)}$ is expressed by the Wiedemann−Franz Law $\kappa_{(carrier)} = L\sigma T$, where L is the Lorenz number.

High-Resolution Transmission Electron Microscopy. The microstructures of $Pb_{9.6}Sb_{0.2}Te_{10-x}Se_x$ samples were examined using high-resolution transmission electron microscopy (HRTEM). Specimens used for the investigation were prepared as follows. Small square-shape pieces with approximate sizes 5 mm × 5 mm × 2 mm were first cut from the ingot using a 50 μm tungsten wire on a wire saw (South Bay Technology Inc.). The samples were then hand-polished with subsequently increasing grit (1000−1500) sand paper to about 200−300 μm in thickness. Circular-shape specimens 3 mm in diameter suitable for use in the TEM sample holder were cut using a Gatan model 601 ultrasonic disk cutter. Samples were then thinned using a Gatan model 656 precession dimple grinder and low-angle ion milled (2°−4°) to electron transparency using a Gatan model 691 precession ion polishing system (PIPS).

The investigation was aimed to provide a reasonable explanation to the reduction of the thermal conductivity of $Pb_{9.6}Sb_{0.2}Te_{10-x}Se_x$ samples compared to those of the corresponding $PbTe_{1-x}Se_x$ solid solution alloys. High-resolution transmission electron microscopy images of several pieces cut from different locations of the ingots were recorded at 200 kV using a JEOL JEM 2200FS (Filed emission TEM). The images were then analyzed by performing the Fast Fourier Transform (FFT) of different area using the program ImageJ.[26]

Results and Discussion

Synthesis. Although the synthesis of the $Pb_{9.6}Sb_{0.2}Te_{10-x}Se_x$ cubic materials seems to be straightforward, small compositional variations in the grown crystals still exist. The composition gradient probably occurs during the cooling process mainly due to the differences in the equilibrium compositions of the liquid and solid phases. The elemental compositions reported here are nominal, but they have been confirmed with energy-dispersive spectroscopy analysis. The X-ray powder diffraction patterns (Figure 1a) indicated that all $Pb_{9.6}Sb_{0.2}Te_{10-x}Se_x$ ($x = 0$ to 10) samples are single phase with NaCl-type structure ($Fm\bar{3}m$). The refined lattice parameters (Figure 1b) showed almost linear contraction with increasing Se content. This is consistent with the isomorphic substitution in the anion positions of larger Te by smaller Se atoms.

---

(22) (a) Wendlandt, W. W.; Hecht, H. G. *Reflectance Spectroscopy*; Interscience Publishers: New York, 1966. (b) Kotuem, G. *Reflectance Spectroscopy*; Springer-Verlag: New York, 1969. (c) Tandon, S. P.; Gupta, J. P. *Status Solidi* **1970**, *38*, 363.

(23) Maldonado, O. *Cryogenics* **1992**, *32*, 908−912.

(24) (a) Loo, S.; Short, J.; Hsu, K.-F.; Kanatzidis, M. G.; Hogan, T. *Mater. Res. Soc. Symp. Proc.* **2004**, *793*, S9.4.1−9. (b) Hogan, T.; Ghelani, N.; Loo, S.; Sportouch, S.; Kim, S.-J.; Chung, D.-Y.; Kanatzidis, M. G. *Proc. Int. Conf. Thermoelectr.* **1999**, 671−674.

(25) *LabVIEW*, version 5.0; National Instruments: Austin, TX, 1999.

(26) Rasband, W. S. *ImageJ*; U.S. National Institutes of Health: Bethesda, Maryland, USA, 1997−2005, http://rsb.info.nih.gov/ij/.

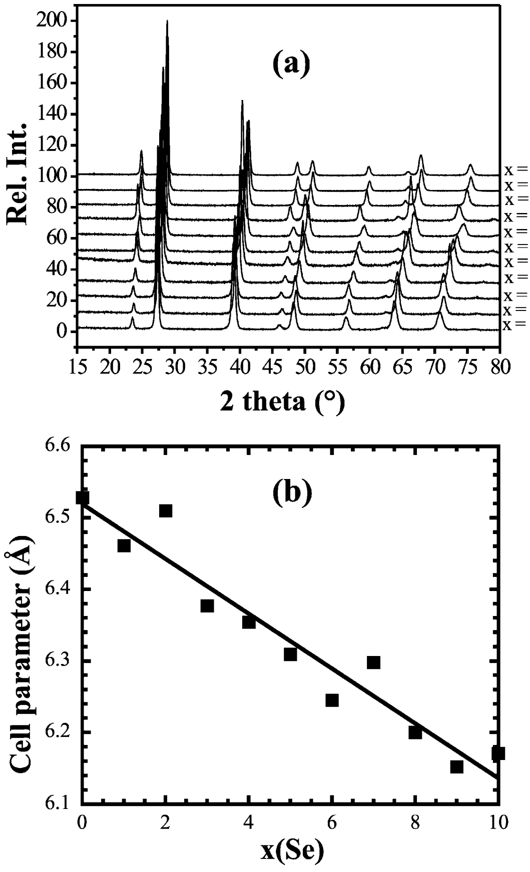

Figure 1. (a) Powder X-ray diffraction patterns of $Pb_{9.6}Sb_{0.2}Te_{10-x}Se_x$ (x = 0 to 10) samples showing the lattice contraction with increasing x (Se). Diffraction patterns were collected using a Cu K_α ($\lambda = 1.540\ 56$ Å) radiation. (b) Variation of the cell parameter (refined from the power patterns) with the Se content (x).

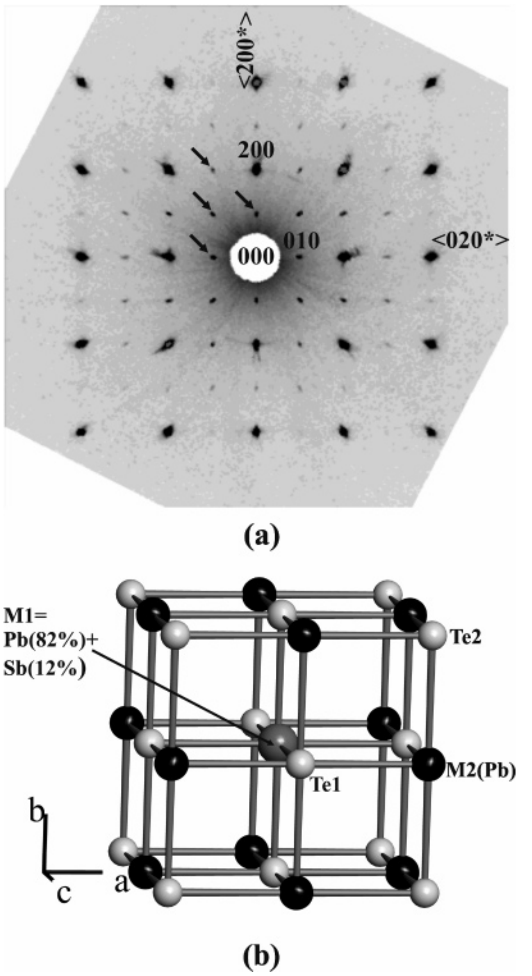

Figure 2. (a) Precession photograph of $hk0$ zone simulated from image plate diffraction data of $Pb_{9.6}Sb_{0.3}Te_{10}$ single crystal. The arrows indicate supplementary Bragg diffraction spots breaking the $Fm\bar{3}m$ symmetry. (b) Average cubic structure of $Pb_{9.6}Sb_{0.3}Te_{10}$ in the space group $Pm\bar{3}m$. The metal position M1 is mixed occupied by Pb and Sb with 6% vacancy.

The structure of $Pb_{9.6}Sb_{0.3}Te_{10}$ combines interesting features such as site vacancy, mixed occupancy, and lower symmetry. This provides flexibility to tune the properties by operating substitutions on selected positions or by filling the vacancy with additional elements. A solid solution series with general formula $Pb_{9.6}Sb_yTe_{10-x}Se_x$ similar to the $PbTe_{1-x}Se_x$ series was generated by substituting Te with Se in anion positions and by varying the Sb content. Preliminary investigations of this system revealed that the electronic properties of the samples strongly depend on the Sb content (y = 0; 0.2; 0.4).[27] The samples with composition $Pb_{9.6}Sb_{0.2}Te_{10-x}Se_x$ ($y = 0.2$) showed a more promising combination of thermopower and electrical conductivity and were deemed more likely to produce materials with an enhanced figure of merit. As we will show later, with increasing Se concentration the Sb solubility in the Pb-sublattice decreases and the $Pb_{9.6}Sb_{0.2}Te_{10-x}Se_x$ materials surprisingly became nanostructured with Sb precipitating to form nanocrystals embedded in a $Pb_{9.6}Sb_zTe_{10-x}Se_x$ (where $z < 0.2$) matrix.

Structure of $Pb_{3.82}Sb_{0.12}Te_4$. Unlike the $Fm\bar{3}m$ symmetry suggested by the powder X-ray diffraction patterns of $Pb_{9.6}Sb_{0.2}Te_{10-x}Se_x$ samples, single-crystal X-ray diffraction of a specimen obtained from a batch of $Pb_{9.6}Sb_{0.2}Te_{10}$ indicated lower symmetry ($Pm\bar{3}m$) and a stoichiometry of $Pb_{3.82}Sb_{0.12}Te_4$. $Pb_{9.6}Sb_{0.3}Te_{10}$ therefore adopts a pseudo NaCl structure type in which the symmetry reduction to $Pm\bar{3}m$ causes the Na and Cl positions to split into two crystallographically independent metal positions and two anion positions. Precession photographs of the $hk0$ zone simulated from experimental diffraction data (Figure 2a) showed additional reflections breaking the F-centering, suggesting the presence of Pb/Sb atomic ordering in the structure. The refinement in the $Pm\bar{3}m$ space group revealed a preferential occupation of both metal positions (Figure 2b). The M1($^1/_2$, $^1/_2$, $^1/_2$) position showed mixed occupancy between Pb and Sb with a total occupancy factor of 94% (i.e., 6% vacancy) while the M2($^1/_2$, 0, 0) position is fully occupied by Pb. The refined occupancy was M1 = 82%Pb + 12%Sb. The average interatomic bond distance of 3.220(1) Å is slightly shorter than the typical value of 3.231 Å found in pure PbTe.[28] This is the first experimental evidence that Sb can occupy a Pb site at a concentration as high as 3%. This result is in contrast to a published phase diagram which indicates a lower solubility of Sb (~1%) into the PbTe lattice. [29]

Thermal Analysis and Energy Band Gap. Differential thermal analysis of $Pb_{9.6}Sb_{0.2}Te_{10-x}Se_x$ (x = 0 to 6) samples

---

(27) Poudeu, P. F. P.; D'Angelo, J.; Downey, A.; Sootsman, J.; Pcionek, R.; Zhou, Z.; Palchik, O.; Hogan, T. P.; Uher, C.; Kanatzidis, M. G. *Mater. Res. Soc. Symp. Proc.* **2006**, *886*, F05-09.1−6.

(28) Bouad, N.; Chapon, L.; Marin-Ayral, R.-M.; Bouree-Vigneron, F.; Tedenac, J. C. *J. Solid State Chem.* **2003**, *173*, 189−195.

(29) Abrikosov, N. Kh.; Skudnova, E. V.; Poretskaya, L. V.; Osipova, T. A. *Inorg. Mater.* **1969**, *5*, 630−633.

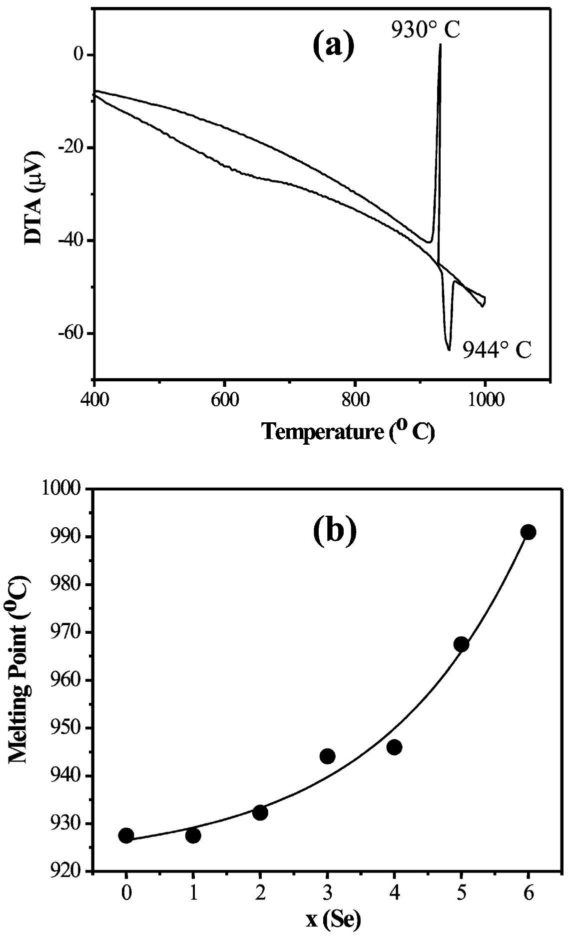

Figure 3. Typical differential thermal analysis (DTA) plot of $Pb_{9.6}Sb_{0.2}Te_{10-x}Se_x$ ($x = 3$). (b) Variation of the melting point of $Pb_{9.6}Sb_{0.2}Te_{10-x}Se_x$ series with the composition (x) (peak temperatures are reported).

show one endothermic peak corresponding to the melting during the heating cycle. A sharp exothermic peak of recrystallization was also observed during the cooling cycle (Figure 3a). The melting point of the $Pb_{9.6}Sb_{0.2}Te_{10-x}Se_x$ series increases monotonically with increasing Se content (Figure 3b). The observed melting points range from 927 °C ($x = 0$) to 991 °C ($x = 6$).[30] This result is in line with the trend observed for the melting points of PbTe (924 °C) and PbSe (1080 °C).

Infrared spectroscopy of $Pb_{9.6}Sb_{0.2}Te_{10-x}Se_x$ ($x = 0$ to 10) samples shows that all members of the series are narrow gap semiconductors. Figure 4a shows a typical absorption spectrum of $Pb_{9.6}Sb_{0.2}Te_{10-x}Se_x$ ($x = 3$) and reveals a sharp well-defined change in the absorption coefficient. The band gaps derived from these plots decrease with increasing Se (x) content (Figure 4b). This result is consistent with the anomalous trend of the energy gap between PbTe and PbSe which have a gap of 0.32 and 0.27 eV, respectively.[31] The energy gaps of $Pb_{9.6}Sb_{0.2}Te_{10}$ (0.31 eV) and $Pb_{9.6}Sb_{0.2}Se_{10}$ (0.27 eV), the two end members of the series as measured in this work, agree well with the values reported for PbTe and PbSe at 300 K.[32]

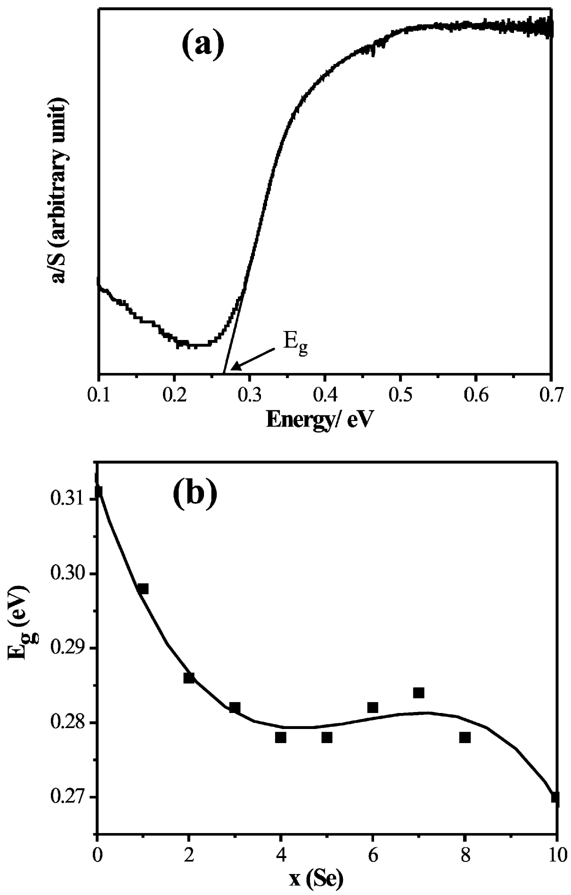

Figure 4. (a) Typical electronic absorption spectrum of $Pb_{9.6}Sb_{0.2}Te_{10-x}Se_x$ ($x = 3$) at room temperature. (b) Variation of the energy gap with the composition (x). The energy gap value is indicated by an arrow. The band gaps range from 0.27 eV ($x = 10$) to 0.31 eV ($x = 0$).

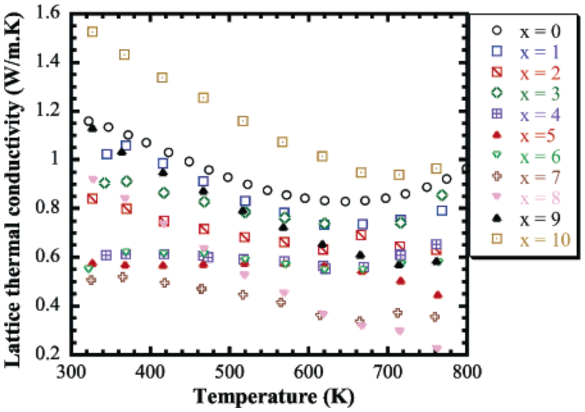

Figure 5. Temperature dependence of the lattice thermal conductivity of $Pb_{9.6}Sb_{0.2}Te_{10-x}Se_x$ ($x = 0$ to 10) samples.

Lattice Thermal Conductivity and TEM Study. Figure 5 shows the temperature dependence of the lattice thermal conductivity (κ_L) of $Pb_{9.6}Sb_{0.2}Te_{10-x}Se_x$. For $x = 0$ ($Pb_{9.6}Sb_{0.2}Te_{10}$), the κ_L value at 300 K is ~1.2 $W{\cdot}m^{-1}{\cdot}K^{-1}$. This corresponds to about a 50% reduction of the typical value of 2.3 $W{\cdot}m^{-1}{\cdot}K^{-1}$ reported for PbTe.[33] The room-temperature value of 1.5 $W{\cdot}m^{-1}{\cdot}K^{-1}$ measured for a sample with $x = 10$ ($Pb_{9.6}Sb_{0.2}Se_{10}$) is similar to the κ_L of pure PbSe.[1] Samples of the $Pb_{9.6}Sb_{0.2}Te_{10-x}Se_x$ ($x = 1$ to 8) solid solution series show

---

(30) Samples with $x > 6$ showed no peak within the operational range of temperature of our Shimadzu DTA-50 thermal analyzer suggesting a melting above 1000 °C.

(31) (a) Wei, S.-; Zunger, A. *Phys. Rev. B* **1997**, *55*, 13605−13610. (b) Dalven, R. *Phys. Rev. B* **1971**, *3*, 3359−3367.

(32) Zemel, J. N.; Jensen J. D.; Schoolar, R. B. *Phys. Rev.* **1965**, *140*, A330−A342.

(33) Ioffe, A. F. *Can. J. Phys. (Paris)* **1956**, *34*, 1342.

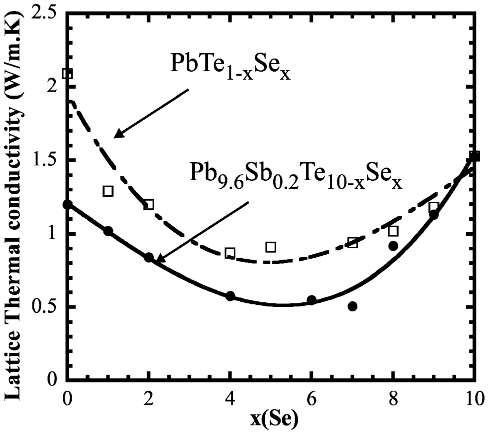

Figure 6. Comparison of the lattice thermal conductivity of $Pb_{9.6}Sb_{0.2}Te_{10-x}Se_x$ with those of the $PbTe_{1-x}Se_x$ standard solid solutions alloy at 300 K.[1]

κ_L values below 1 $W{\cdot}m^{-1}{\cdot}K^{-1}$ at room temperature. The lattice thermal conductivity of $Pb_{9.6}Sb_{0.2}Te_{10-x}Se_x$ samples attains a minimum between 600 and 700 K (Figure 5). This behavior was also found in several heavily doped PbTe-based semiconductors,[11,14,15,34] and it corresponds to the transition from the extrinsic to the intrinsic region.[34]

More interestingly, samples with compositions $Pb_{9.6}Sb_{0.2}Te_{10-x}Se_x$ ($x = 4, 6, 7$) show extremely low values of lattice thermal conductivity. For $x = 4$ and 6, the room-temperature values are ~0.6 $W{\cdot}m^{-1}{\cdot}K^{-1}$ and remain constant with increasing temperature. This corresponds to about two-thirds of the values measured for the $PbTe_{1-x}Se_x$[1] solid solution series for an equivalent amount of Se. The composition with $x = 7$ shows the lowest lattice thermal conductivity ~0.5 $W{\cdot}m^{-1}{\cdot}K^{-1}$ at 300 K which decreases further to 0.4 $W{\cdot}m^{-1}{\cdot}K^{-1}$ at 750 K. This value of the lattice thermal conductivity is very close to a value of 0.35 $W{\cdot}m^{-1}{\cdot}K^{-1}$ at 300 K reported for the very high ZT $PbSe_{0.98}Te_{0.02}$/PbTe superlattice thin films.[10]

Figure 6 shows the relationship between the composition (x) and the room-temperature values of the lattice thermal conductivity of $Pb_{9.6}Sb_{0.2}Te_{10-x}Se_x$ and for comparison $PbTe_{1-x}Se_x$[1] solid solutions. The lattice thermal conductivity of all $Pb_{9.6}Sb_{0.2}Te_{10-x}Se_x$ samples is lower than the corresponding solid solution and decreases with increasing x (Se) to a minimum ($x = 7$) and then starts increasing for higher Se content. For an equivalent amount of Se, the lattice thermal conductivity of $Pb_{9.6}Sb_{0.2}Te_{10-x}Se_x$ ($x < 8$) samples are 30 to 40% lower that those of the $PbTe_{1-x}Se_x$ standard solid solution alloys.

The lattice thermal conductivity depends on the phonon transport through the crystal.[35] It can however be reduced by phonon scattering, which is caused by a large mass fluctuation disorder in one atomic position of the crystal structure and also by quantum nanodots embedded in the samples.[36−40] Our results strongly suggest that in addition to the well-known atomic disorder between Te and Se atoms that is believed to be responsible for the reduction of the lattice thermal conductivity in the $PbTe_{1-x}Se_x$ solid solutions, a new phonon scattering mechanism that is responsible for further suppression of phonon transport is taking place in the $Pb_{9.6}Sb_{0.2}Te_{10-x}Se_x$ samples. This

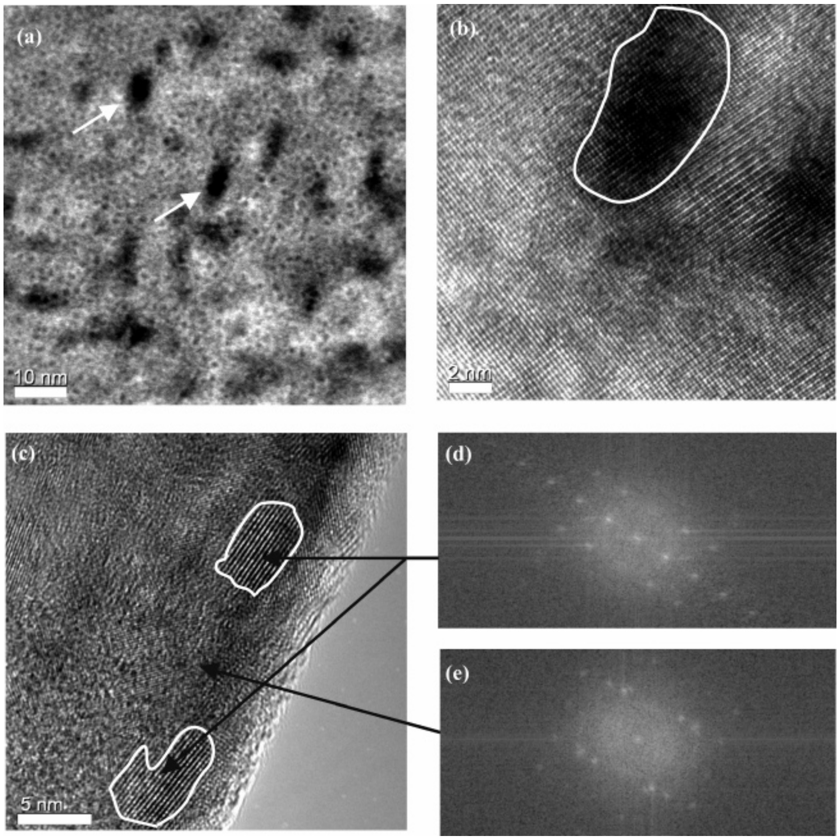

Figure 7. (a) Low magnification TEM of $Pb_{9.6}Sb_{0.2}Te_7Se_3$ showing Sb-rich nanocrystals of various sizes and shapes embedded inside PbTe-rich matrix. (b) High-resolution image (HRTEM) of a selected portion of $Pb_{9.6}Sb_{0.2}Te_7Se_3$ sample showing an ~5 nm large nanocrystal embedded inside PbTe-rich matrix. (c) High-resolution image (HRTEM) showing the coexistence of domains with different features. The fast Fourier transform (FFT) of both domains showed smaller periodicity for the islands (Figure 6d) compared to the bulk matrix (Figure 6e).

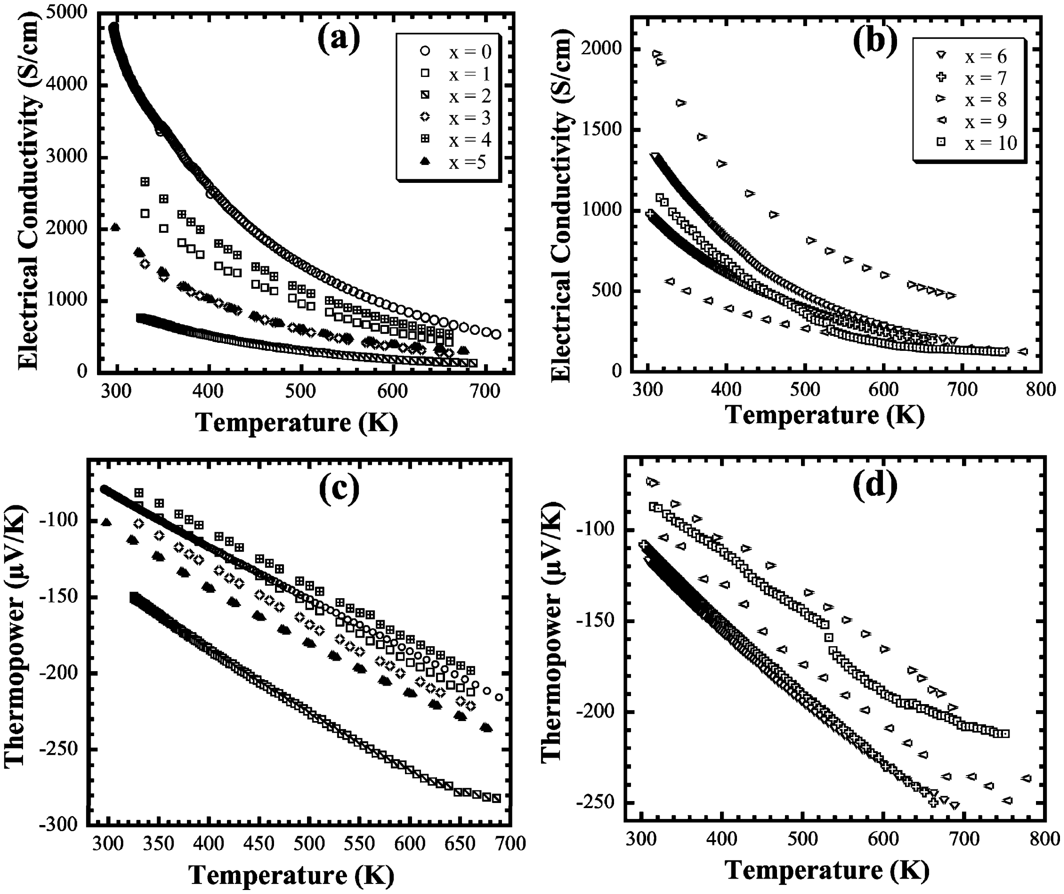

Figure 8. Temperature dependence of electrical properties of $Pb_{9.6}Sb_{0.2}Te_{10-x}Se_x$ ($x = 0$ to 10) samples. (a and b) Electrical conductivity; (c and d) Thermopower.

prompted us to perform HRTEM on several members of $Pb_{9.6}Sb_{0.2}Te_{10-x}Se_x$ ($x = 2$, 3, and 4). HRTEM images from all ingots showed similar features, and therefore we only show images from the samples of composition $Pb_{9.6}Sb_{0.2}Te_7Se_3$. The images of $Pb_{9.6}Sb_{0.2}Te_7Se_3$ showed several characteristics we believed are favorable to the strong suppression of the lattice thermal conductivity observed in the $Pb_{9.6}Sb_{0.2}Te_{10-x}Se_x$ materials. For instance, the low magnification TEM image of $Pb_{9.6}Sb_{0.2}Te_7Se_3$ depicted in Figure 7a clearly shows nanocrystals of varying sizes and shapes that are embedded and dispersed inside the PbTe-rich matrix. Both the large size distribution and the high dispersion of the nanocrystals are favorable to the scattering of a wide phonon spectrum (mid-to-long wavelength) and therefore contribute significantly to the alteration of the lattice thermal conductivity. The nanocrystals are formed during the cooling process from the natural phase segregation between PbTe and Sb and are believed to be Sb-rich. This compositional fluctuation is accompanied by the formation of crystal boundaries (Figure 7b and 7c) due to the slight lattice mismatch between regions with different compositions.

Long wavelength phonons are effectively scattered at the crystal boundaries, and the scattering effect is enhanced in systems where the constituents have large differences in atomic mass.[41] In addition, domains with different atomic spacings cocrystallized at the nanometer scale (Figure 7c). The fast Fourier transform (FFT) of both domains showed smaller periodicity for the islands (Figure 7d) compared to the matrix (Figure 7e). Therefore, the islands could be regarded as Sb-rich regions. The abundance of such nanocrystals inside the sample may be the key feature favorable to the high suppression of the lattice thermal conductivity of $Pb_{9.6}Sb_{0.2}Te_{10-x}Se_x$ materials. A recent study of the thermoelectric properties of PbTe alloyed with Sb_2Te_3 shows a significant reduction of the lattice thermal conductivity arising from the fact that the donor action of the Sb substituting Pb is not compensated by the acceptor action of the vacancies formed in the lattice.[42] We suspect that nanostructuring is responsible for this observation as well.

Electrical Properties. Figure 8a and b show the temperature dependence of the electrical conductivity of $Pb_{9.6}Sb_{0.2}Te_{10-x}Se_x$ samples. Regardless of composition, the electrical conductivity monotonically decreased with increasing temperature, indicating degenerate conduction for the whole measuring temperature range. The temperature dependence is in accordance with the power law $T^{-\delta}$, where the power exponent δ ranges from

---

(34) (a) Orihashi, M.; Noda, Y.; Chen, L.-D.; Goto, T.; Hirai, T. *J. Phys. Chem. Solids* **2000**, *61*, 919−923. (b) Orihashi, M.; Noda, Y.; Chen, L.-D.; Goto, T.; Hirai, T. *Mater. Trans., JIM* **2000**, *41*, 1196−1201.

(35) (a) Goldsmid, H. J.; Penn, A. W. *Phys. Lett.* **1968**, *A27*, 423. (b) Savvides, N.; Goldsmid, H. J. *J. Phys. (Paris)* **1980**, *C13*, 4657. (c) Sharp, J. W.; Poon, S. J.; Goldsmid, H. J. *Phys. Status Solidi A* **2001**, *187*, 507−516.

(36) Sales, B. C.; Chakoumakos, B. C.; Mandrus, D.; Sharp, J. W. *J. Solid State Chem.* **1999**, *146*, 528−432.

(37) Khitun, A.; Wang, K. L.; Chen, G. *Nanotechnology* **2000**, *11*, 327−331.

(38) Majumdar, A. *Science* **2004**, *303*, 777−778.

(39) Li, D.; Huxtable, S. T.; Abramson, A. R.; Majumdar, A. *J. Heat Transfer* **2005**, *127*, 108−114.

(40) Tritt, T. M.; Subramanian, M. A. *MRS Bulletin* **2006**, *31*, 188−194.

(41) Zhu, P. W.; Imai, Y.; Isoda Y.; Shinohara, Y.; Jia, X.; Zou, G. *J. Phys.: Condens. Matter* **2005**, *17*, 7319−7326.

(42) Zhu, P. W.; Imai, Y.; Isoda Y.; Shinohara, Y.; Jia, X.; Zou, G. *J. Phys.: Condens. Matter* **2005**, *17*, 7319−7326.

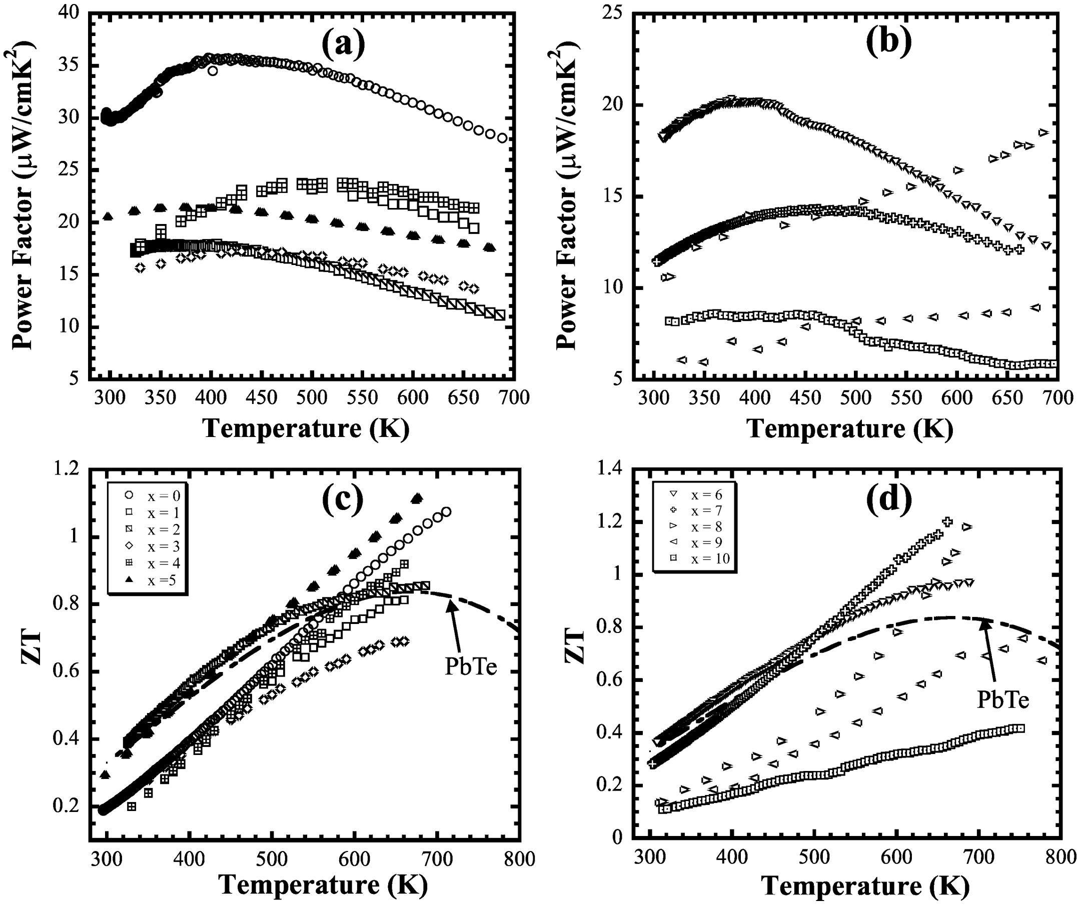

Figure 9. (a and b) Temperature dependence of power factor of $Pb_{9.6}Sb_{0.2}Te_{10-x}Se_x$ ($x = 0$ to 10) samples. (c and d) Comparison of the calculated figures of merit of $Pb_{9.6}Sb_{0.2}Te_{10-x}Se_x$ ($x = 0$ to 10) samples with the state-of-the-art n-type PbTe.

1.84 to 2.27. The value of δ decreases with increasing carrier density. For example, the electrical conductivity of the sample with composition $x = 0$ with a room-temperature conductivity of 4800 S/cm falls according to $T^{-2.27}$ law, while the composition $x = 9$ with an electrical conductivity of 700 S/cm at 300 K follows $T^{-1.84}$ law. The power law dependence of the electrical conductivity (also found in PbTe) results from the phonon scattering of charge carriers.[43]

It is important to stress here that no systematic trend was found in the variation of the electrical conductivity of $Pb_{9.6}Sb_{0.2}Te_{10-x}Se_x$ samples with the selenium content. For instance, compositions with $x = 0$, 1, and 4 exhibit room-temperature electrical conductivities above 2000 S/cm, while other samples show room-temperature conductivities between 600 and 2000 S/cm. The observed behavior can be due to inhomogeneities, microscopic cracks, or more importantly the difference of doping levels in $PbTe_{1-x}Se_x$ solid solution when alloying with ~1 at. % Sb.

All samples showed negative values of the thermopower over the entire temperature range indicating n-type conduction (Figure 8c and d) consistent with the donor property of Sb sitting on Pb sites in the structure. Regardless of composition, the thermopower of $Pb_{9.6}Sb_{0.2}Te_{1-x}Se_x$ samples increases almost linearly with temperature, with samples of low Se content showing sharper slopes. Most samples show thermopower values ranging from −80 μV/K at 300 K to −220 μV/K at 650 K. Ingots with composition $Pb_{9.6}Sb_{0.2}Te_8Se_2$ ($x = 2$) showed the highest values of the thermopower (Figure 8c). At 300 K the thermopower was −150.9 μV/K and increased smoothly to −282 μV/K at 700 K.

The temperature-dependent power factor ($\sigma \cdot S^2$) plots for $Pb_{9.6}Sb_{0.2}Te_{10-x}Se_x$ samples are compared in Figure 9a and b. At room temperature, all samples show high values of the power factor. For sample with $x = 0$, the power factor at 300 K is about 30 μW/cm·K^2. As the temperature increases, the power factor reaches a maximum of 35 μW/cm·K^2 around 400 K. Compositions with $x = 1$ and 4 exhibit a maximum power factor of 24 μW/cm·K^2 around 500 K. For $x = 2$, 3, 5, 6, and 7, the power factor plots decrease with rising temperature after reaching a maximum around 450 K. For the composition $x = 8$, the power factor increases with the temperature and reaches a maximum of 17 μW/cm·K^2 near 650 K. Samples with higher Se content showed a poor power factor. For instance, the $x = 9$ sample showed a power factor of ~5 μW/cm·K^2 at 300 K and reached a maximum of 9 μW/cm·K^2 at 650 K. The sample with $x = 10$ showed a higher power factor of ~8 μW/cm·K^2 at 300 K, but it decreases rapidly with rising temperature.

The temperature-dependent figures of merit (ZT) for $Pb_{9.6}Sb_{0.2}Te_{10-x}Se_x$ calculated from the above data are compared in Figure 9c and d together with n-type PbTe.[44] At 300 K all $Pb_{9.6}Sb_{0.2}Te_{10-x}Se_x$ samples (except the composition with $x = 2$) showed ZT values below that of the state-of-the-art n-type

---

(43) Ravich, Y. I.; Efimova, B. A.; Smirnov, I. A. *Semiconducting Lead Chalcogenides*; Plenum Press: New York, London, 1970.

(44) Heikes, R. R.; Ure, R. W. *Thermoelectricity: Science and Energy*; Interscience: New York, 1961.

PbTe (ZT ≈ 0.3). However, their temperature dependence was very different. For the composition $Pb_{9.6}Sb_{0.2}Te_{10}$ ($x = 0$), the ZT at 300 K is only about 0.2 despite a huge power factor of ~30 μW/cm·K^2. This is due to the large value of the total thermal conductivity resulting from the extremely high electrical conductivity. As the temperature increased, the ZT rises almost linearly reaching the performance of PbTe (ZT = 0.8) near 550 K. At 700 K a maximum ZT of 1.1 was achieved. This value is ~40% higher than that of doped PbTe and is comparable to the value 1.16 reported for PbTe alloyed by 0.8 mol % Sb_2Te_3.[42] The samples with $x = 2, 4, 5, 6, 7$, and 8 also showed an improved figure of merit compared to PbTe. For $x = 2$, a maximum ZT of 0.82 was obtained at 700 K. Compositions with $x = 4, 5, 6$, and 8 achieved a maximum ZT of 0.93, 1.17, 0.96, and 1.18 respectively at 700 K.

The most impressive enhancement of ZT was observed for the sample with $x = 7$ (Figure 9d). The sample with composition $Pb_{9.6}Sb_{0.2}Te_3Se_7$ exceeded PbTe around 500 K and reached the highest ZT of 1.20 around 650 K. This corresponds to about a 50% enhancement of the figure of merit of PbTe at 650 K. This large improvement of the ZT of $Pb_{9.6}Sb_{0.2}Te_3Se_7$ (compared to PbTe) is due to its extremely low lattice thermal conductivity ($\kappa_L \approx 0.4$ W/m·K at 750 K) coupled to an optimal electrical conductivity and thermopower. A high-temperature extrapolation of the linear temperature dependence ZT plot of $Pb_{9.6}Sb_{0.2}Te_3Se_7$ indicates a possible figure of merit of 1.5 at 800 K.

Concluding Remarks

The system $PbTe_{1-x}Se_x$, with and without Sb added, presents an excellent case where the effects of solid solution alloying to the reduction in thermal conductivity can be decoupled from those of nanostructuring. Therefore it provides an opportunity to assess the additional influence of the latter. The $Pb_{9.6}Sb_{0.2}Te_{10-x}Se_x$ solid solution series behaves very differently from the classical $PbTe_{1-x}Se_x$ series of solid solution in regard to phonon transport. The lattice thermal conductivities of $Pb_{9.6}Sb_{0.2}Te_{10-x}Se_x$ ($x \leq 8$) samples at 300 K are significantly lower than that of $PbTe_{1-x}Se_x$ for an equivalent amount of Se. This reduction in the lattice thermal conductivity is attributed to the formation of Sb-rich nanocrystals inside the samples and provides an additional phonon scattering mechanism over and above the standard point defect scattering mechanism that typically governs solid solutions. As a result, a maximum ZT of ~1.20 at 650 K was achieved for composition $Pb_{9.6}Sb_{0.2}Te_3Se_7$. This value is about 50% higher than that of the state-of-the-art n-type PbTe.

Acknowledgment. Financial support from the Office of Naval Research (Contract No. N00014-02-1-0867 MURI Program and N00014-06-1-0130) is greatly acknowledged.

Supporting Information Available: X-ray crystallographic data in CIF format for the single-crystal refinement of $Pb_{3.82}Sb_{0.12}Te_4$. This material is available free of charge via the Internet at http://pubs.acs.org.

JA0647811